Oxygen-deficient photostable Cu_2O for enhanced visible light photocatalytic activity†

Mandeep Singh,‡[a] Jampaiah Deshetti,*‡[a] Ahmad E. Kandjani,[b] Ylias M. Sabri,[b] Enrico Della Gaspera, [c] Philipp Reineck,[d] Martyna Judd,[e] Julien Langley,[e] Nicholas Cox, [e] Joel van Emdben,[c] Edwin Mayes,[f] Brant C. Gibson,[d] Suresh K. Bhargava, [b] Rajesh Ramanathan [a] and Vipul Bansal *[a]

Oxygen vacancies in inorganic semiconductors play an important role in reducing electron–hole recombination, which may have important implications in photocatalysis. Cuprous oxide (Cu_2O), a visible light active p-type semiconductor, is a promising photocatalyst. However, the synthesis of photostable Cu_2O enriched with oxygen defects remains a challenge. We report a simple method for the gram-scale synthesis of highly photostable Cu_2O nanoparticles by the hydrolysis of a Cu(I)-triethylamine [Cu(I)–TEA] complex at low temperature. The oxygen vacancies in these Cu_2O nanoparticles led to a significant increase in the lifetimes of photogenerated charge carriers upon excitation with visible light. This, in combination with a suitable energy band structure, allowed Cu_2O nanoparticles to exhibit outstanding photoactivity in visible light through the generation of electron-mediated hydroxyl (OH·) radicals. This study highlights the significance of oxygen defects in enhancing the photocatalytic performance of promising semiconductor photocatalysts.

Introduction

Semiconductor photocatalysis represents an efficient way to utilize solar energy, and as such, offers a promising avenue for next-generation green technologies, including the production of clean energy and efficient environmental management.[1–4] Semiconducting titanium dioxide (TiO_2) remains the most extensively investigated photocatalyst due to its high chemical stability, low toxicity, low cost, and commercial availability.[5]

[a]Ian Potter NanoBioSensing Facility, NanoBiotechnology Research Laboratory, School of Science, RMIT University, Melbourne, VIC 3000, Australia. E-mail: vipul.bansal@rmit.edu.au, jampaiah.deshetti@rmit.edu.au

[b]Centre for Advanced Materials and Industrial Chemistry, School of Science, RMIT University, Melbourne, VIC 3000, Australia

[c]School of Science, RMIT University, Melbourne, VIC 3000, Australia

[d]ARC Centre of Excellence for Nanoscale BioPhotonics, School of Science, RMIT University, Melbourne, VIC 3000, Australia

[e]ARC Centre of Excellence for Nanoscale BioPhotonics, School of Science, RMIT University, Melbourne, VIC 3000, Australia

[f]Research School of Chemistry, Australian National University, Canberra, ACT 2601, Australia

However, the large band gap (3.2 eV) and high recombination rates of charge carriers in TiO_2 mean that it practically works well only in the ultraviolet (UV) spectral range.[6–8] Considering that the UV component corresponds to only ~3% of the solar irradiation reaching the earth's surface,[9,10] there has been an ongoing pursuit for new catalysts that are visible light active, possess a direct narrow band gap, and have high photochemical stability.

Cuprous oxide (Cu_2O), a p-type semiconductor, offers a narrow direct band gap (E_g of 2.1–2.6 eV) that is coupled with the appropriate positioning of its conduction band just above the reduction potential of water.[11–14] These desirable semiconductor properties, in combination with high natural abundance, low toxicity, and low cost of copper, make Cu_2O a promising material for visible light-driven applications, such as photocatalysis, photovoltaics and photoelectrochemical devices.[15–17] However, to realise the true potential of Cu_2O, limitations such as its stability during synthesis and storage, photostability during catalysis, and synthesis of oxygen-deficient Cu_2O need to be addressed.

Notably, the high chemical activity of Cu_2O, which is an advantage for photocatalysis, arises from the +1 oxidation state of Cu, which can either be reduced to Cu^0 or oxidised to Cu^{2+} thereby facilitating redox reactions efficiently. However, this brings an associated drawback, i.e. Cu_2O is very prone to rapid oxidation into cupric oxides (CuO and Cu_4O_3).[18] This poses

significant challenges not only to produce phase-pure Cu_2O under mild conditions in large quantities,[11] but also to retain the photoactive Cu_2O phase without its oxidation to dramatically less-active cupric oxides during photocatalysis.[19]

The other major challenge associated with photoactive Cu_2O is that irrespective of the synthesis conditions, copper vacancies have been found to be the most stable defect states, whereas the synthesis of oxygen-deficient Cu_2O remains challenging.[20] However, the presence of oxygen vacancies in semiconductor photocatalysts has been demonstrated to offer remarkable potential in photocatalysis by suppressing charge carrier recombination processes.[21–23]

Herein, we demonstrate a new aqueous phase approach that allows the gram-scale synthesis of highly oxygen-deficient Cu_2O nanoparticles under ambient conditions. The ease of synthesis offered by our approach provides potential opportunities to produce this important photocatalyst at an industrial scale. We overcome the synthesis challenge associated with stable phase-pure Cu_2O nanoparticles *via* addressing the well-known problem of the instability of inorganic Cu(I) salts in water due to the higher lattice and solvation energies for the Cu^{1+} ion over those of Cu^{2+} ions.[24] As such, this problem typically results in the rapid disproportion of Cu^{1+} ions into Cu^{2+} and Cu^0 in an aqueous environment as per eqn (1):[25]

$$2Cu^+ \rightarrow Cu^{2+} + Cu^0 \qquad (1)$$
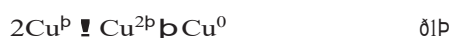
A few selected soft organic ligands, in particular, *N*-methylated ligands, have the ability to stabilize transition metals in low valence states through forming a hydrophobic complex with the metal ions.[26] For instance, in 1963, Tollin and co-workers reported the synthesis of low melting Cu(I) complexes through a 1 : 1 melt reaction between amine-based soft ligands and copper chloride salts.[27] These complexes had either a linear structure with coordination number 2 or a tetrahedral structure with coordination number 4, and it was noted that the complexes with coordination number 2 could be synthesised with a strongly basic or easily polarisable ligand. Such complexes with strongly basic or easily polarisable ligands exhibit low vapour pressures due to electrostatic interactions between the polarised ligand and the metal ion.[27,28]

In our investigations, we employed triethylamine (Et_3N, TEA) as a highly basic polarisable tertiary amine (pK_a – 10.75) to initially form a Cu(I)–TEA complex. The spontaneous hydrolysis reaction of this Cu(I)–TEA complex with water at 80 °C then produced spherical Cu_2O nanoparticles on the gram scale (2.56 g per batch) with over 90% conversion yield from the precursor copper salts. This is important considering that the scale-up synthesis of nanomaterials is typically difficult, yielding only few micrograms to milligrams of materials per batch under standard unoptimized laboratory conditions. Furthermore, since Cu_2O nanoparticles are typically prone to surface oxidation, we carefully studied the photostability, crystal structure, defect states, and presence of oxygen vacancies in these Cu_2O nanoparticles. Additionally, the energy band structure and charge recombination lifetimes of

Cu_2O nanoparticles were obtained, which was followed by assessing their ability to photocatalytically oxidise eco-toxic environmental pollutants, such as a coloured methyl orange dye and the colourless tetracycline under visible light illumination and simulated solar irradiation. Overall, the present study not only provides a facile protocol to achieve the large-scale synthesis of photostable, oxygen-deficient Cu_2O nanoparticles but also emphasises the significance of oxygen vacancies in semiconducting photocatalysts for enhancing their photocatalytic performance.

Results and discussion

The schematic in Fig. 1 provides a summary of the gram-scale process used for the synthesis of oxygen-deficient Cu_2O nanoparticles. The first critical step is to obtain a Cu(I)–TEA complex through the spontaneous reaction of copper(II) chloride with TEA in acetonitrile at 80 °C (see Experimental section for details). While the formation of stable coordination complexes of Cu(I) species was first studied over 50 years ago,[27–29] to our surprise, such complexes have not yet been explored to produce difficult-to-synthesize Cu_2O nanoparticles. It has been noted that among various primary, secondary and tertiary amines, the latter form stable metal complexes with transition metal ions, due to the strong coordination bond between the metal and the tertiary amines.[29] We chose TEA as a model tertiary amine to act as a coordinating agent for the formation of a Cu(I)–TEA complex. The reaction mechanism involved in the formation of the Cu(I)–TEA complex is believed to be initiated through a redox mechanism involving one electron transfer process giving rise to a dichlorocuprate(I) anion and a radical cation *via* a series of reaction intermediates (eqn (2) and (3)). These radical ions may co-exist in equilibrium with other copper(I) complexes of TEA.

$$CuCl_2 + NEt_3 \rightarrow [CuCl_2]^- [NEt_3]^+ \qquad (2)$$

$$[CuCl_2]^- [NEt_3]^+ \rightleftharpoons [CuCl][NEt_3] + Cl \qquad (3)$$
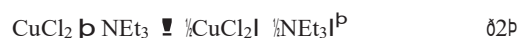
We propose that this Cu(I)–TEA complex offers a new promising approach to produce Cu_2O nanoparticles in large quantities. This is because the high basicity of the TEA molecules (pK_a – 10.75) pre-complexed with Cu(I) should allow the

Fig. 1 Schematic representation of the large-scale production of Cu_2O nanoparticles.

spontaneous hydrolysis of this complex in water to form Cu_2O (eqn (4)).

$$2\{CuCl\}\!\!\frac{1}{2}NEt_3\} + H_2O \longrightarrow Cu_2O + 2NEt_3 + 2HCl \qquad (4)$$

When the Cu(I)−TEA complex is mixed with water at 80 °C, a yellowish-orange colloid begins to form instantaneously. After 4 hours of reaction, 2.56 grams of vacuum-dried Cu_2O powder is collected from a single batch that corresponds to a yield of over 90% of the precursor copper ions.

To understand the crystal growth mechanism of Cu_2O formation, time-dependent experiments were conducted at room temperature (instead of 80 °C to slow down the thermal-driven kinetics). We retrieved the colloidal product after 10 s, 30 s, 1 min, 2 min, and 4 min of the reaction and analysed their morphology by transmission electron microscopy (TEM) after rapidly drying-off the TEM samples under vacuum (Fig. 2). After 10 s, the majority of the structures were in the form of long interlaced nanotubes with an average diameter of ∼5 nm and a length over 100 nm. Within 30 s, these nanotubes formed closely packed structures, some resembling quasi-spherical morphologies. As the reaction progressed, the wrapping of these interlaced nanotubes continued, such that within 4 min, only quasi-spherical particles averaging 50−200 nm in diameters, comprised of ensembles of nano-tubes, were observed. High-resolution TEM (HRTEM) imaging of the nanotubes revealed an interplanar spacing of 0.24 nm, consistent with the (111) lattice plane of cubic Cu_2O (Fig. S1, ESI†). Interestingly, even at this early time point of the reaction, we didn't observe the formation of any intermediate copper hydroxide phase. This supports that the hydrolysis of a Cu(I)−TEA complex by water leads to the spontaneous formation of interlaced tubular structures of Cu_2O, which then rapidly evolve into spherical morphologies.

The morphology, size, and crystallinity of these quasi-spherical Cu_2O nanostructures were investigated by electron microscopy. Fig. 3a shows a representative high resolution scanning electron microscopy (SEM) image of the Cu_2O nanostructures, suggesting their overall quasi-spherical morphology formed through ensembles of multiple ultra-small particles. These ensembles showed an average diameter of 150 nm, as evident from the particle size distribution obtained from SEM
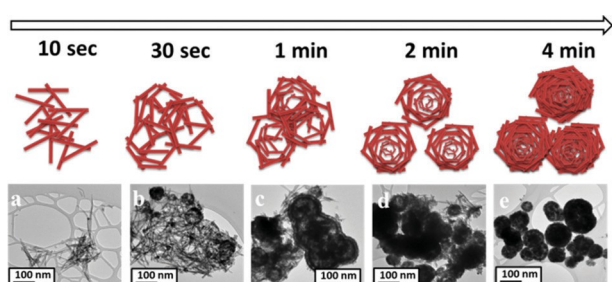

Fig. 3 (a) SEM, (b) TEM, (c) SAED pattern, and (d−f) HR-TEM images of Cu_2O nanoparticles along with (g, h) the corresponding lattice fringe distribution in a defect-free highly crystalline area and a defect-rich area, respectively, as marked with yellow lines in panels (e) and (f). The inset in (e) shows a fast Fourier transform (FFT) of the red highlighted region.

Fig. 2 Schematic illustration of the morphological evaluation of Cu_2O nanoparticles and the corresponding TEM images over reaction times of (a) 10 s, (b) 30 s, (c) 1 min, (d) 2 min and (e) 4 min at room temperatu
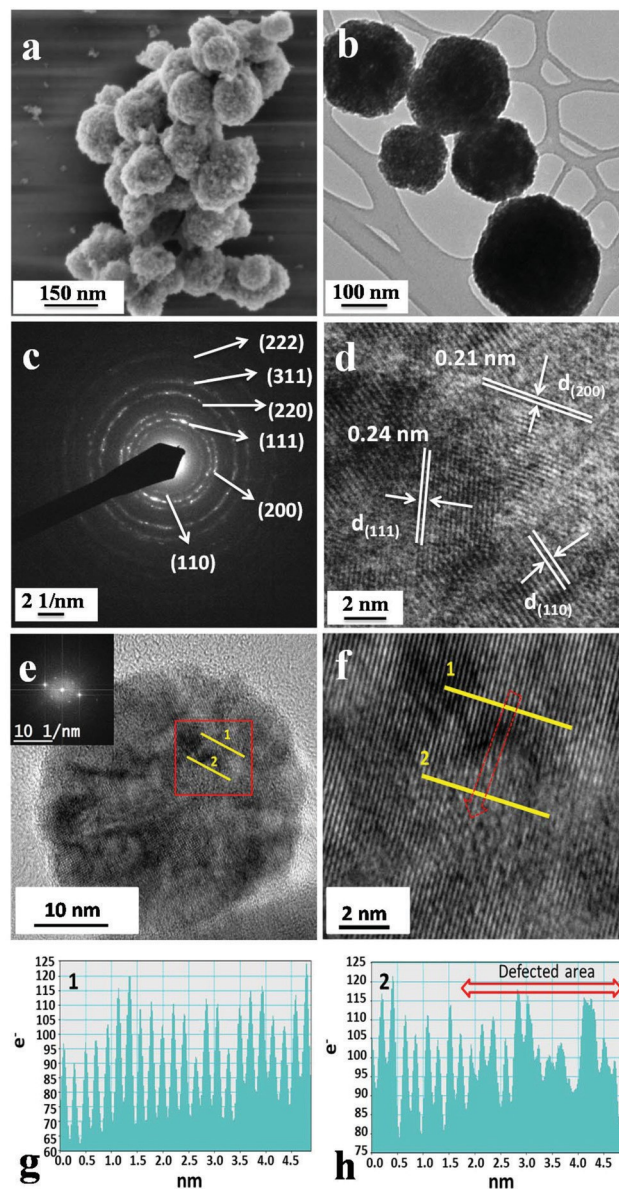
(Fig. S2, ESI†). The dynamic light scattering (DLS) analysis revealed consistent results with a narrow size distribution and an average hydrodynamic diameter of 340 nm (Fig. S3, ESI†). The TEM image further confirms the quasi-spherical morphology containing an ensemble of several ultra-small particles within a larger particle of 100−200 nm diameters (Fig. 3b). The corresponding selected area electron diffraction (SAED) pattern from these particles confirms their high crystallinity with well-defined (110), (111), (200), (220), (311) and (222) diffraction planes corresponding to the cubic phase of Cu_2O (Fig. 3c). The high-resolution EDX mapping further

affirms the presence of Cu and O in these particles (Fig. S4, ESI†).

High-resolution TEM (HR-TEM) images reveal clear lattice fringes with interplanar spacings of 0.24, 0.21 and 0.29 nm that are consistent with the (111), (200), and (110) planes of cubic phase Cu_2O (Fig. 3d).[30] We also noticed the presence of irregular regions in the form of discontinued lattice fringes on the surface of Cu_2O crystals (Fig. 3e–h). These features suggest that a highly defect-rich Cu_2O structure might have formed during crystal transformation from nanorods to nanospheres. Interestingly, the fast Fourier transform (FFT) of the region containing both ordered and discontinuous lattices (inset of Fig. 3e) showed that irrespective of the presence of defects, the overall crystallinity of the region remained as cubic Cu_2O. As such, these defects within the Cu_2O crystal are likely to induce localized copper and oxygen vacancies, which may have important implications for their optical and resultant photocatalytic properties, as investigated later.

While HRTEM studies provide strong evidence that the prepared material is cubic Cu_2O, in general, it is extremely challenging to stabilise pure copper(I) oxide under ambient conditions. Therefore, we employed a number of complementary techniques to investigate the oxidation state of copper in these nanoparticles. Electron paramagnetic resonance (EPR) spectroscopy offers an ideal avenue to assess the oxidation state of copper. We performed continuous wave (CW) X-band EPR measurements on Cu_2O nanoparticles, and compared the EPR spectrum with that of the liquid Cu(I)–TEA complex (the precursor for Cu_2O synthesis) and the Cu(II) sulphate EPR standard (Fig. S5, ESI†). It is noted that in X-band EPR, only copper centers in the +2 oxidation state should be visible. As the dominant oxidation state of copper centers in the Cu(I)–TEA complex as well as in Cu_2O nanoparticles is expected to be +1, it is expected that both these samples should be EPR silent or only exhibit weak Cu(II) signals. In contrast, the $CuSO_4$ standard should generate a strong Cu(II) signal. As expected, $CuSO_4$ generated a typical EPR signal, representative of Cu(II). Interestingly, the Cu(I)–TEA complex, which we expected to be EPR silent, also generated a Cu(II) signature. A comparison of the double integral EPR signal measured for the Cu(I)–TEA precursor and the $CuSO_4$ standard demonstrates that the proportion of the precursor in the +2 oxidation state is rather low, of the order of 2%. We believe that this feeble Cu(II) signature in the Cu(I)–TEA complex is most likely due to the complex equilibrium kinetics that takes place during Cu(I)–TEA synthesis among multiple intermediates, as represented in a simplified form through eqn (2) and (3). In contrast, the EPR profile of Cu_2O nanoparticles suggests that it is unlikely that the spectrum represents a single species, but instead a distribution. The overall EPR profile of Cu_2O, with positive peaks *ca.* g = 2.4, and a more narrow feature at *ca.* g = 2, is characteristic of Cu(II) in a tetragonally elongated octahedral/square planar ligand field. A further resolved peak below g = 2 indicates a sub-population with a different coordination (trigonal/tetrahedral). This is also true for the Cu(I)–TEA precursor spectrum, although its hyperfine structure is unresolved.

A comparison of the EPR signals of Cu_2O nanoparticles with the $CuSO_4$ standard after factoring in changes in the instrument settings, temperature and normalisation based on the total copper in each sample reveals that the EPR signal for Cu_2O nanoparticles is less than 1% of that of the standard. These results thus support the notion that the Cu(II) concentration in Cu_2O nanoparticles is indeed very small. Since Cu(I)–TEA also showed Cu(II) signals, and other complementary techniques did not show any features of Cu(II) oxides, we believe that the weak Cu(II) signals from Cu_2O nanoparticles are most likely due to the unhydrolysed Cu(I)–TEA complex that may act as a capping agent to stabilise Cu_2O nanoparticles during synthesis.

Furthermore, since Cu_2O is generally prone to surface oxidation during storage, to assess their ambient stability over the long term, we analysed a Cu_2O nanoparticle 8 weeks post-synthesis using high-angle annular dark-field scanning transmission electron microscopy (HAADF-STEM), and fine-structure electron energy loss spectroscopy (EELS) as a line profile across the particle length (Fig. 4). The O K edge from the particle shows a prominent peak at 532.5 eV, confirming the presence of the cubic Cu_2O phase.[31] Importantly, the peak positions of the fine structures of Cu L3 and L2 energy edges are representative of the oxidation state of this transition element.[32] The observed Cu L3 edge at 933.4 eV remains consistent across various locations within a single particle (zones 1–6). This is representative of the Cu^{1+} oxidation state,[31]
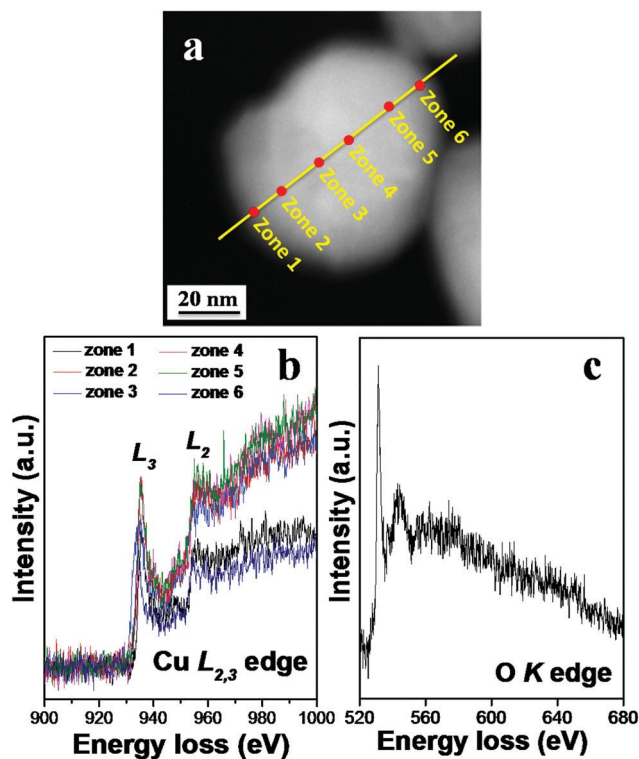

Fig. 4 (a) HADDF-STEM image of a Cu_2O nanoparticle with the corresponding EELS spectra of the (b) Cu L2,3 and (c) O K edges.

further confirming that our nanoparticles remain stable in the pure crystalline phase of Cu_2O under ambient conditions.

The crystallinity and phase purity of Cu_2O nanoparticles are further evident from their powder X-ray diffraction (XRD) analysis and comparison with a commercial Cu_2O nanopowder (Fig. S6a, ESI†). Both materials show characteristic diffraction lines at 30.2, 37.1, 43.0, 62.1, 74.5, and 78.5° corresponding to the (110), (111), (200), (220), (311) and (222) lattice planes of the cubic structure of Cu_2O (ICDD No. 05-0667), respectively.[33] The absence of other diffraction peaks supports the lack of any potential impurity in the material. In comparison with the commercial Cu_2O, the as-synthesised nanoparticles showed broader diffraction peaks, supporting that the particle domains are in the nanoscale range. The crystallite size of as-synthesised Cu_2O nanoparticles (12.8 ± 4.1 nm) calculated based on the Scherer equation was found to be over six times smaller than that of commercial Cu_2O (68.2 ± 17.9 nm). The average crystallite size of 12.8 nm for as-synthesised Cu_2O nanoparticles further supports that the larger spheres of *ca.* 150 nm diameter observed during electron microscopy are composed of ultra-small Cu_2O nanoparticles. Furthermore, N_2 porosimetry studies to compare the surface area of Cu_2O nanoparticles with the commercial powder (Fig. S6b, ESI†) revealed that the Cu_2O nanoparticles synthesised using a $Cu(I)$−TEA complex showed a type III N_2 sorption isotherm with a high volume of N_2 absorbed. In contrast, the commercial Cu_2O showed a negligible amount of N_2 absorption. As such, our material showed over an order of magnitude higher BET surface area (42 m^2 g^{-1}) compared to its commercial counterpart (4 m^2 g^{-1}). This higher

surface area of Cu_2O nanoparticles prepared in our study is likely to be advantageous through providing more number of active surface sites for photocatalytic processes.

To investigate the defect states in Cu_2O nanoparticles, we simultaneously studied the confocal Raman and photoluminescence (PL) properties of the particles using a Horiba LabRAM HR evolution Raman spectrometer, performed X-ray photoelectron spectroscopy (XPS) on these particles, and compared them with the commercial counterpart (Fig. 5). The Raman spectrum of commercial Cu_2O nanoparticles shows a characteristic major peak at *ca.* 219 cm^{-1}, along with some low-intensity features (Fig. 5a). The strong vibrational band at 219 cm^{-1} is characteristic of Cu_2O and corresponds to the second order overtone $2\Gamma_{12}$ mode.[34] In the case of as-synthesised Cu_2O nanoparticles, the $2\Gamma_{12}$ mode is slightly shifted to 217 cm^{-1}.[35] The additional Raman peaks in Cu_2O nanoparticles at 92, 148, 416, 520, and 632 cm^{-1} can be ascribed to a combination of defects, non-stoichiometry, and resonant excitations.[36] In particular, the 148 cm^{-1} feature is attributed to Γ_{15} oxygen vacancies (LO), and its high intensity in as-synthesised Cu_2O nanoparticles confirms the presence of a large number of oxygen defects in the Cu_2O lattice.[37] As such, the Raman spectrum of nanoscale Cu_2O confirms a highly defect-rich material, in which the high intrinsic mobility of oxygen and copper species within an asymmetric Cu−O stretching and an asymmetric O−Cu−O bending environment offers great promise for photocatalysis applications.[38]
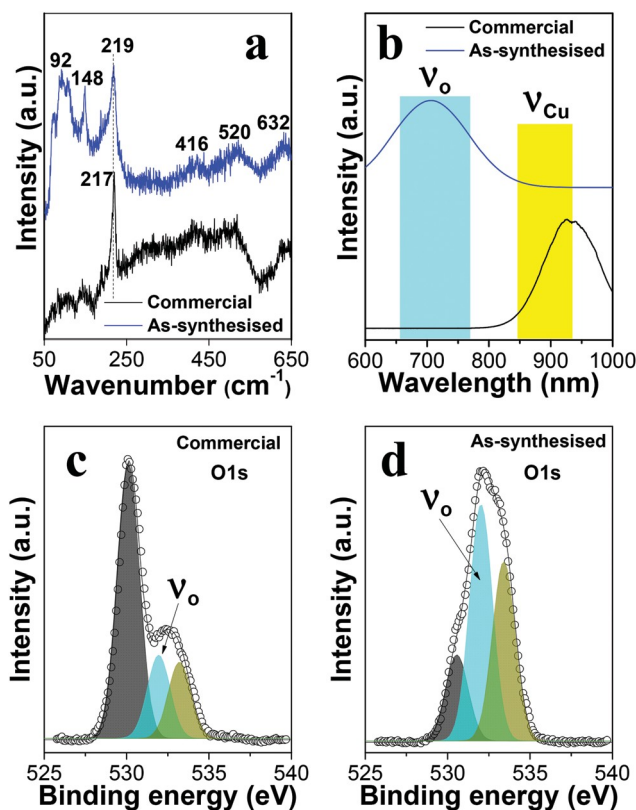

Fig. 5 Comparison of the (a) confocal Raman, (b) PL and (c, d) O 1s core–shell spectra of as-synthesised Cu_2O nanoparticles with the commercial counterpart. v_O and v_{Cu} correspond to oxygen and copper vacancies, respectively.

The presence of oxygen defects in our material was further confirmed by PL spectroscopy, as the relative position of the emission peak is indicative of the defect states in Cu_2O (Fig. 5b).[39,40] The as-synthesised Cu_2O nanoparticles exhibited a predominant peak at 706 nm that is attributable to the recombination of excitons bounded to oxygen vacancies (v_O) in the cubic Cu_2O lattice.[39] This observation supports that the morphological transformation process observed during nanorod to nanosphere transition led to intrinsic oxygen defects during synthesis. In contrast, the commercial Cu_2O nanoparticles did not show PL signature at *ca.* 700 nm, but instead showed a strong feature at 928 nm that corresponds to the emission from excitons bounded by copper vacancies (v_{Cu}) in the lattice.[40]

In addition to Raman and PL spectroscopy, the O 1s core level XPS spectra of the commercial (Fig. 5c) and as-synthesised (Fig. 5d) Cu_2O nanoparticles further affirm that our nanoparticles are rich in oxygen vacancies. As such, the O 1s spectrum in each case could be resolved into three distinct components with binding energies maxima 529, 530.1, and 531.8 eV that are attributed to the oxygen present in the Cu_2O lattice, oxygen associated with an oxygen vacancy (v_O) environment, and the ambient oxygen adsorbed on the surface of particles arising from water or carbonate species, respectively. Out

of the total oxygen available within the Cu₂O lattice, the relative amount of oxygen vacancy concentration in as-synthesised Cu₂O nanoparticles corresponds to *ca.* 73%, while only 23% oxygen vacancies were found in commercial Cu₂O. While commercial Cu₂O is predominantly rich in copper vacancies, as evident from PL spectroscopy (Fig. 5b), the co-existence of a certain degree of oxygen vacancies in the commercial material is not surprising.

Altogether, these spectroscopic investigations provide strong evidence that while commercial Cu₂O is highly copper-deficient, the nanostructured Cu₂O reported in this study is predominantly oxygen-deficient. The presence of oxygen vacancies in a semiconductor has been observed to offer remarkable potential in suppressing the electron and hole recombination processes, thereby enhancing the photo-absorption capacity of the material.[41] As such, the enhanced formation of oxygen vacancies in nanostructured Cu₂O reported here could provide similar benefits in promoting photocatalytic performance.

The optical band gap of these oxygen-deficient Cu₂O nanoparticles was obtained from the optical absorption measurements (Fig. 6a) using Tauc's plot (Fig. 6b)[42] with the following eqn (5).

$$A = \frac{k(h\nu - E_g)^{n=2}}{h\nu} \tag{5}$$

where A is the absorbance, k is a constant, h is the Planck's constant, ν is the frequency, and n equals 1 for direct transitions. The obtained direct band gap (E_g) value of 2.45 eV for Cu₂O nanoparticles is in good agreement with the literature (2.1–2.6 eV).[33] In comparison, the commercial Cu₂O showed a band gap of 2.1 eV. It is likely that the larger band gap of our material is due to the presence of defects and resultant deviation from a perfect stoichiometry. As such, this wider energy gap is more suitable to reduce the recombination rate of the charge carriers during photocatalysis. Furthermore, this band gap edge of 2.45 eV (corresponding to 506 nm wavelength) is suitable for visible light-induced photostimulation.
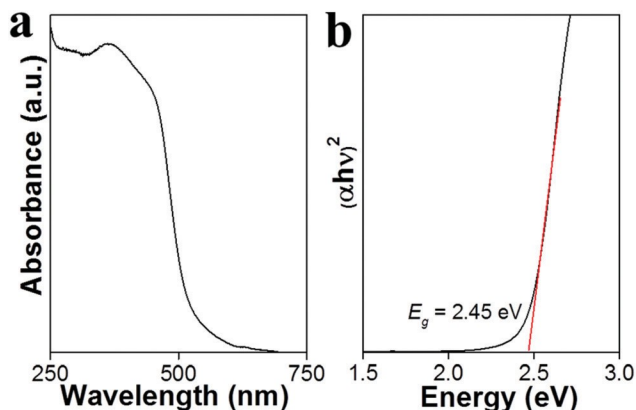
Next, we evaluated the photocatalytic performance of oxygen-deficient Cu₂O nanoparticles through studying a model reaction involving the photooxidative degradation of methyl orange (MO) under visible light illumination. The pristine MO molecules show a strong absorption peak at 463 nm, and their photodegradation can be monitored by evaluating the reduction in the absorbance intensity using UV-Vis absorption spectroscopy.[43–46] C_t/C_0 was used to compare the photocatalytic performance of the spherical Cu₂O nanoparticles and the bulk counterpart (C_0 is the initial concentration of MO, and C_t is the concentration at time t). Fig. 7a shows the photocatalytic degradation of MO over 15 min in the presence of as-synthesised oxygen-deficient Cu₂O nanoparticles under visible light illumination. The insert shows that within 15 min, the intense orange colour of MO completely disappears due to the high visible light photoactivity of Cu₂O nanoparticles. The kinetics of MO degradation by Cu₂O nanoparticles under visible light irradiation is further compared with the commercial Cu₂O nanoparticles in Fig. 7b and c. Control experiments in the absence of the catalyst show that MO itself cannot be
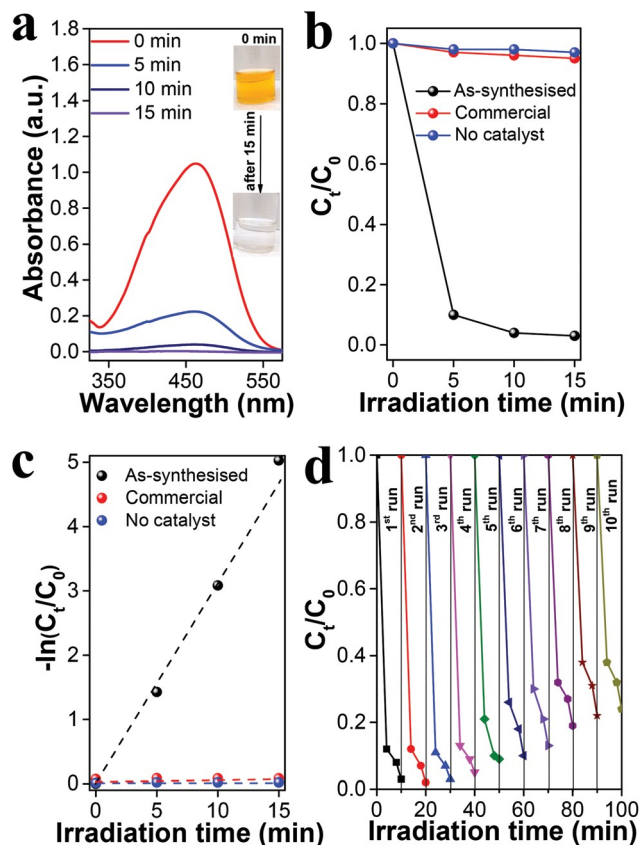

Fig. 7 (a) Absorption spectra of MO after visible light photo-irradiation in the presence of oxygen-deficient Cu₂O nanoparticles – insets show MO solution at the initial and end time points; (b) plots of C_t/C_0 *vs.* irradiation time depicting the photodegradation of MO in the presence of different catalysts; (c) plots of $-\ln(C_t/C_0)$ *vs.* irradiation time used to calculate the reaction rate constants; and (d) recycling test of oxygen-deficient Cu₂O nanoparticles under visible light irradiation for 10 cycles of MO photodegradation.

Fig. 6 (a) UV-vis absorption spectrum and (b) Tauc's plot of Cu₂O nanoparticles. The black curves are experimental spectra and the red curve is the fitted spectrum.

degraded under visible light. The reaction in the presence of light followed pseudo-first order kinetics. The as-synthesised oxygen-deficient Cu_2O nanoparticles led to the near complete photodegradation of the MO molecules with an extremely high rate constant of 0.334 min^{-1}. In contrast, the commercial counterpart could not promote MO degradation (rate constant of 0.519×10^{-3} min^{-1}). We believe that this difference of three orders of magnitude in the photoactivity is most likely due to the poor dispersibility and low surface area of the commercial Cu_2O nanoparticles that might have further reduced during the experiments *via* aggregation. In comparison, our nanoparticles remained highly dispersible and offered appropriate band gap for visible photoexcitation. The stability studies of as-synthesised Cu_2O nanoparticles during multiple cycles of reaction revealed $\sim 80\%$ of photoactivity retention over 10 cycles (Fig. 7d). The observed gradual loss of activity ($\sim 20\%$) may be partially due to the loss of Cu_2O nanoparticles during post-reaction harvesting and re-use over multiple cycles. In contrast, the commercial Cu_2O nanoparticles showed very poor reusability with less than 15% of the original catalytic performance retained in the second cycle. This loss of activity in commercial Cu_2O is due to their poor photostability and rapid oxidation to CuO and other higher oxidation state copper oxides within one cycle of photocatalysis, as evident from XRD analysis (Fig. S7, ESI†). On the other hand, the as-synthesised oxygen-deficient Cu_2O nanoparticles retain their cubic phase purity even after repeated exposure to ten cycles of photocatalysis reactions (Fig. S8, ESI†). These results, in combination with long-term EELS stability studies (Fig. 4), provide strong evidence that oxygen-deficient Cu_2O nanoparticles prepared using the new Cu(I)–TEA hydrolysis route reported here have outstanding photostability under ambient as well as visible light illumination conditions.

We further assessed the prospects of oxygen-deficient Cu_2O nanoparticles in degrading other organic environmental pollutants by investigating the photooxidative degradation of tetracycline in visible light (Fig. S9, ESI†). In the absence of a catalyst, tetracycline could not be degraded, indicating the importance of a suitable catalyst for its photodegradation. The commercial Cu_2O could degrade only 7% tetracycline, whereas the oxygen-deficient Cu_2O showed $\sim 90\%$ degradation efficiency within 20 min of visible light irradiation.

Convinced with the high photostability and photocatalytic activity of oxygen-deficient Cu_2O nanoparticles, we further evaluated its performance under solar illumination conditions simulated for equator daylight (Fig. S10, ESI†). The MO molecules completely degraded within 1 hour, leading to the decolouration of the resultant solution. These observations confirm that the photostable Cu_2O nanoparticles offer remarkable potential as an efficient visible light photocatalyst for the practical harvesting of solar energy.

To obtain mechanistic insights into oxygen-deficient Cu_2O-driven photocatalysis, we determined the position of the conduction band (CB), valence band (VB), Fermi level (E_f), associated band gap energy (E_g), and the lifetime stability of the photogenerated charge carriers, all of which synergistically

play important roles in determining the overall photocatalytic performance of semiconductors. The excitation of an electron from VB to CB of a semiconductor photocatalyst can only occur if the optical radiation energy is equal to or greater than the E_g. Once the electron (e^-) is photoexcited to the CB, it leaves a hole (h^+) at the VB, and the separation efficiency of these charged carriers dictates the overall photocatalytic performance. The oxygen-deficient Cu_2O nanoparticles reported in this study have a direct optical band gap of 2.45 eV (Fig. 6b), which makes them photoactive under visible light. Thus, the VB and CB potentials of the Cu_2O nanoparticles are measured through eqn (6) and (7):[47]

$$E_{VB} = X + 0.5E_g - E_e \qquad (6)$$

$$E_{CB} = E_{VB} - E_g \qquad (7)$$

where E_{VB} is the valence band edge potential, X is the electronegativity of the semiconductor, E_e is the energy of free electrons *versus* hydrogen (4.5 eV), E_g is the band-gap energy of the semiconductor, and E_{CB} is the conduction band edge potential. The calculated CB and VB potential values of Cu_2O nanoparticles w.r.t. to a nascent hydrogen electrode (NHE) correspond to -0.42 (E_{CB}) and 2.03 eV (E_{VB}), respectively.

Furthermore, the Fermi level position for oxygen-deficient Cu_2O nanoparticles was determined to be 0.29 eV above the E_{VB} from the valence band XPS by using the intercept of the tangent to the density of states at the Fermi edge (Fig. S11, ESI†). The relevant energy band positions of p-type semiconductor Cu_2O nanoparticles are presented in Fig. 8 suggesting that upon photoexcitation with visible light, electrons (e^-) and holes (h^+) will be photogenerated (eqn (8)). These electrons will have sufficient potential to reduce the molecular O_2 to produce the superoxide anion ($O_2^{\cdot-}$), as the CB edge potential of Cu_2O nanoparticles is located at -0.42 eV (*vs.* NHE), while the required O_2 reduction potential is -0.28 eV.[12] These $O_2^{\cdot-}$ radicals can then undergo a series of reductive reactions to produce H_2O_2 (eqn (9)) and $OH^\cdot$ radicals (eqn (10) and (11)). These $OH^\cdot$ radicals can then participate in
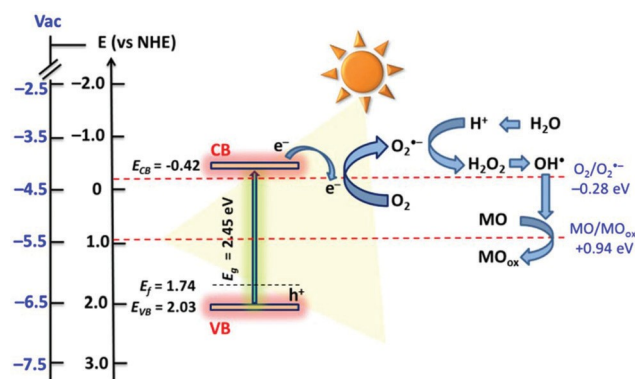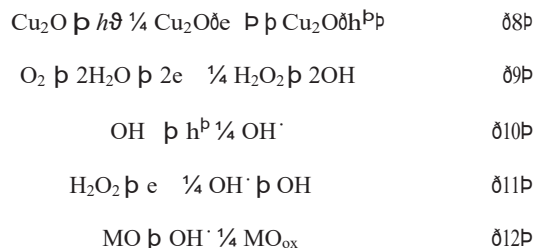

Fig. 8 Schematic representation of the energy band diagram of Cu_2O nanoparticles, showing their ability to be photoexcited with visible light to generate $OH^\cdot$ radicals that actively participate in the photooxidation of MO molecules.

the photooxidation of MO *via* eqn (12), due to a favourable MO redox potential (0.94 eV).[48]

$$Cu_2O + h\vartheta = Cu_2O(e^- + h^+)$$ (8)

$$O_2 + 2H_2O + 2e^- = H_2O_2 + 2OH^-$$ (9)

$$OH^- + h^+ = OH^·$$ (10)

$$H_2O_2 + e^- = OH^· + OH^-$$ (11)

$$MO + OH^· = MO_{ox}$$ (12)

To validate the photo-induced production of $O_2^{·-}$ and $OH^·$ radicals, EPR spectroscopy involving spin trap experiments was performed (Fig. S12, ESI†). The spin trap used was 5,5-dimethyl-pyrroline *N*-oxide (DMPO), as DMPO allows the detection of both superoxide and hydroxyl radicals. In such experiments, these radical species are detected by their reaction with the initially EPR-silent DMPO. It is noted that the DMPO-OH$^·$ and DMPO-OOH$^·$ adducts give rise to two different EPR signals. To test the quality of our DMPO stock solutions and the performance of our illumination setup, control measurements of the photodecomposition of H_2O_2 into $OH^·$ radicals were performed. In the control DMPO solution, a negligible concentration of the DMPO-OH$^·$ adduct is observed. Upon the addition of oxygen-deficient Cu_2O nanoparticles in the dark, a stable population of the DMPO-OH$^·$ adduct was formed. Illumination of the Cu_2O/DMPO reaction mixture for 15 min with white light led to a roughly 2-fold increase in the DMPO-OH adduct signal. The photo-induced DMPO-OH$^·$ adduct EPR signal was observed to decay in the dark over the course of an hour. The signal could however be regenerated upon further white light illumination. The DMPO-OOH$^·$ adduct was not observed in any sample. The EPR spin trap experiments strongly support our above hypothesis that the photo-induced production of $OH^·$ radicals upon the photo-excitation of oxygen-deficient Cu_2O nanoparticles is predominantly responsible for the observed outstanding photocatalytic activity of this material. The photo-induced production of $OH^·$ radicals is further evident from an experiment involving terephthalic acid (TA) as a $OH^·$ radical-specific fluorogenic probe that is readily converted into a highly fluorescent 2-hydroxy terephthalic acid in the presence of photoexcited Cu_2O nanoparticles (Fig. S13, ESI†).[49]

To validate the role of these oxidative species in the degradation of MO molecules, we studied the photocatalysis performance of oxygen-deficient Cu_2O nanoparticles in the presence of ethylenediaminetetraacetic acid (EDTA) and tertiary butyl alcohol (TBA), which act as scavengers for electrons and $OH^·$ radicals, respectively (Fig. S14, ESI†). Both these scavengers were able to significantly suppress the photooxidative efficiency of Cu_2O nanoparticles, affirming the role of $OH^·$ radicals in the Cu_2O-driven visible light photocatalysis.

The recombination dynamics of the photogenerated charge carriers was investigated from the time-resolved photoluminescence (TRPL) spectrum of Cu_2O nanoparticles using a pulsed laser and measuring the corresponding PL decay times
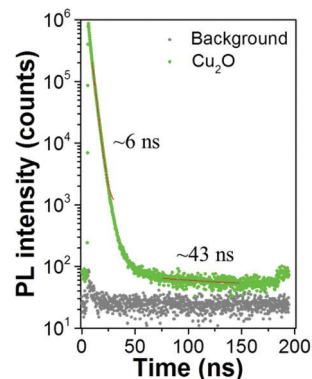

Fig. 9 Time-resolved photoluminescence (TRPL) decay transients for oxygen-deficient Cu_2O nanoparticles.

(Fig. 9). The instrument response function (IRF) is shown in Fig. S15 (ESI†), confirming the ability of the instrument to resolve a few nanoseconds decay. The TRPL spectrum shows a multi-exponential decay behaviour with at least two very distinct fluorescence lifetimes (τ) − one of the order of few nanoseconds, and the other of the order of 40 nanoseconds. While the τ of the order of 1−5 nanoseconds is typically observed for semiconductor photocatalysts,[50,51] it is uncommon to observe such extremely long-lived states leading to carrier lifetimes of an order of higher magnitude. This signifies the importance of oxygen vacancies present in Cu_2O nanoparticles in acting as deep trap sites and thereby assisting in the efficient separation of the charge carriers.

To further validate the recombination efficiency of charge carriers, we performed transient photoelectrochemical (PEC) measurements on oxygen-deficient Cu_2O nanoparticle-based devices prepared on a conducting FTO substrate. Initially, we obtained open circuit photocurrents by exciting Cu_2O films with different wavelengths of light (Fig. 10a). The chosen LED light sources included 470 nm ($E_{ex} > E_g$), 525 nm ($E_{ex} \approx E_g$), and 623 nm ($E_{ex} < E_g$) to represent various photoexcitation scenarios. Upon exposure to the same light intensities (500 μW cm^{-2}), the highest photocurrent densities were obtained when the surface was illuminated with 470 nm wavelength. As expected, the other two low energy sources could not efficiently photoexcite Cu_2O, thereby showing relatively lower responses. The current density response profiles over 10 on/off repeat cycles showed a repeatability of >98% at all wavelengths, once again reaffirming the high photostability of Cu_2O nanoparticles prepared in this study (Fig. S16, ESI†). Further experiment involving the exposure of Cu_2O devices to different intensities of 470 nm wavelength showed a consistent increase in current output with increasing light density (Fig. 10b). This signifies the importance of light intensity in promoting charge carrier separation during photoexcitation. We also performed electrochemical impedance spectroscopy (EIS) at the open circuit potential of 0 V for investigating the influence of photoexcitation on charge transfer and carrier recombination at the Cu_2O/solution interface (Fig. 10c).[52] The
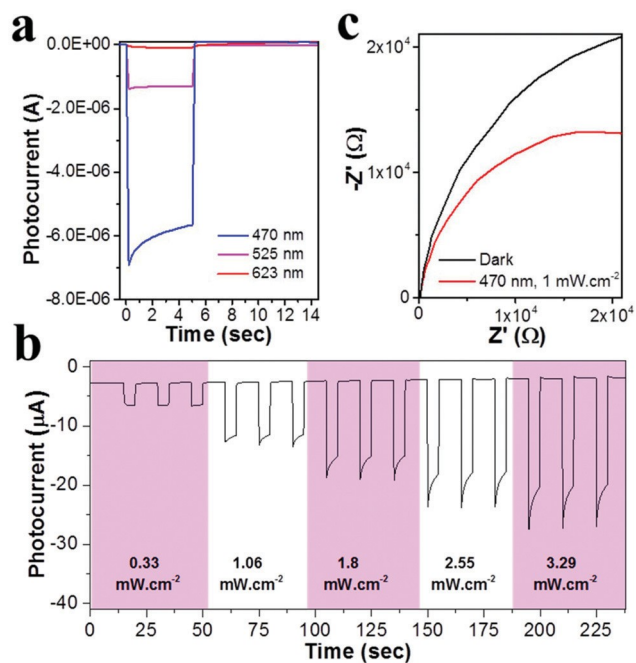
Fig. 10 Photoelectrochemical characterisation showing (a) normalised (w.r.t. dark current) photocurrent response at different wavelength illumination while keeping the light intensity constant at 500 µW cm^{-2}; (b) transient photocurrent density under chopped illumination of 470 nm at 0 V potential *vs.* Ag/AgCl reference electrode involving 5 s-on and 10 s-off intervals in each exposure cycle; and (c) EIS spectra with and without 470 nm (1 mW cm^{-2}) illumination under a DC potential of 0.5 V.

EIS responses are shown as Nyquist plots which involve observing the imaginary part Z'' *versus* the real part Z' of the complex impedance Z. In Nyquist plots, the diameter of the semicircle is proportional to the resistance to charge transfer encountered by the semiconductor. The comparison of the EIS response of Cu_2O devices under dark and photoilluminated conditions reveals that when photoexcited with a 470 nm LED, the diameter of the loop decreases. This supports the visible light-driven photoexcitation of electrons to the CB, thereby promoting the photoactivity of oxygen-deficient Cu_2O nanoparticles.

Conclusions

In summary, we have for the first time, shown the ability to synthesise highly photostable and oxygen-deficient Cu_2O nanoparticles using a low-temperature method. This method allows the production of Cu_2O nanoparticles in gram scale with over 90% yield by a simple water-mediated hydrolysis of a $Cu(I)$−TEA complex. This material could be stored for long periods without oxidising to other copper oxides. As such, these findings are highly significant for the industrial applications of this important p-type semiconductor photocatalyst. Importantly, the presence of an appropriate energy band structure that allows the efficient generation of photocarriers upon excitation with visible light, and a highly oxygen-deficient

Cu_2O lattice that increases the longevity of these charge carriers play a synergistic role in achieving outstanding photocatalytic activity. Overall, an effective route to synthesize oxygen defect-rich Cu_2O in large quantities is likely to find substantial applications in photo-driven processes such as environmental remediation and energy conversion/storage devices.

Experimental section

Materials

Copper(II) chloride ($CuCl_2$), triethylamine (TEA), acetone, methanol, ethanol, acetonitrile, methyl orange, tetracycline and 5,5-dimethyl-pyrroline *N*-oxide (DMPO) were purchased from Sigma-Aldrich, AR grade and used as received. Deionized water (MilliQ, 18.2 MΩ cm) was used for all the experiments.

Synthesis of a Cu(I)−TEA complex

Cu_2O nanoparticles were synthesized by employing a metal co-ordination complex formed between the copper and TEA species in a biphasic solvent mixture of acetonitrile and water. The Cu(I)−TEA metal coordination complex was prepared by the magnetic stirring (500 rpm) of copper(II) chloride (0.1 M in 400 mL acetonitrile) in a round bottom flask at 80 °C for 5 minutes. Following this, 50 mL of TEA was added at once to the above stirring solution. The mild reducing ability of TEA resulted in a reduction of Cu(II) species to Cu(I), which instantaneously formed an ionic complex with TEA. The formation of this Cu(I)−TEA complex was evident from the generation of non-violent vapours upon the addition of TEA to the copper salt. With continuous stirring for 1 hour, the solution phase turned to dark-red. After being cooled to room temperature under ambient conditions, the reaction product was centrifuged at 9000 rpm for 15 minutes to remove any potentially precipitating species. The liquid phase corresponding to the Cu(I)−TEA complex was collected and subsequently used for the synthesis of Cu_2O nanoparticles.

Synthesis of Cu_2O nanoparticles

For the large-scale synthesis of Cu_2O nanoparticles, 450 mL of the purified Cu(I)−TEA complex was brought to 80 °C in a round bottom flask. After 5 minutes, an equivalent volume of water (pre-heated to 80 °C) was added to this complex, which resulted in the instantaneous hydrolysis of the Cu(I)−TEA complex, leading to the precipitation of Cu_2O nanoparticles. The particles were allowed to precipitate for 4 hours under non-stirring conditions. Following this, the reaction contents were allowed to cool for 1 hour, and the Cu_2O nanoparticles were collected by centrifugation at 9000 rpm for 15 minutes. The particles were further washed three times with acetone/methanol (1 : 1 v/v) to obtain a yellow pellet. The precipitate was dried under vacuum at room temperature to achieve a gram-scale (2.56 g) yield of Cu_2O particles in a single batch, which corresponds to over 90% conversion of the starting copper salt.

Materials characterization

The particle size, morphology, and crystallinity of Cu_2O nanoparticles were determined by FE-SEM, as well as TEM and HR-TEM. EDX analysis was performed on a FEG-Varios SEM instrument operated at 15 kV. TEM images were obtained on a JEOL 1010 instrument, operated at 100 kV accelerating voltage. HR-TEM images and SAED patterns were obtained on a JEOL 2100F microscope operating at 200 kV accelerating voltage. EELS was performed in STEM mode on a JEOL 2100F instrument. Multiple EELS spectra were recorded along the surface of Cu_2O particles to validate its oxidation state across the particle surface. For EELS analysis, the intensity ratio of Cu L3 and L2 edges, as well as the O K edge, was used. A Malvern Zeta sizer Nano ZS analyser instrument was used to obtain the hydrodynamic size of the Cu_2O nanoparticles. The crystallinity of Cu_2O was determined by using a Bruker D8 Discover micro-diffraction system with a Cu Kα (1.514 Å) radiation source. The 2θ values in the range of 10−80° were obtained with a 0.021° step size. The determined crystalline phases were indexed based on the International Centre for Diffraction Data-Powder Diffraction File (ICDD-PDF). The crystallite size of the particles was calculated using the Scherer equation based on all of the diffraction peaks of Cu_2O. Specific surface areas (S_{BET}) of Cu_2O nanoparticles were determined by nitrogen (N_2) sorption isotherms at $-196\,°C$ using a Brunauer−Emmett−Teller (BET) analysis method on a Micromeritics (ASAP 2000) analyser. Raman and PL measurements were performed on a Horiba LabRAM HR evolution Raman spectrometer using a 532 nm laser source. The UV-Vis absorbance measurements of an aqueous suspension of Cu_2O nanoparticles were carried out using an Agilent Cary 7000 UV-Vis-NIR spectrophotometer equipped with an integrating sphere. XPS measurements were performed on a K-alpha spectrometer (Thermo Scientific) using a monochromatic Al-Kα (1486.7 eV) radiation source at room temperature under ultra-high vacuum (10^{-8} Pa). TRPL experiments were performed using a custom-built scanning confocal fluorescence microscope with a 100× objective (NA = 0.9) operating at room temperature. A tunable and pulsed (6 ps fundamental pulse-width) white light laser (Fianium, WhiteLaseSC 400) was used to excite particles at 500 nm with a repetition rate of 5 MHz. Photons were collected with avalanche photodiodes (APD, Excelitas, SPCM-AQRH-14) and analysed with a correlator card (Picoquant, TimeHarp 260).

EPR measurement

CW-X-Band EPR spectra were recorded using a commercial Bruker E500 spectrometer equipped with an ER4122 SHQ resonator. Low temperature (20 K) experiments were performed using an Oxford Instruments ESR 935 cryostat and ITC503 temperature controller. Frozen solution and solid powder samples were loaded into standard X-band EPR tubes of 3.8 mm I.D. Liquid solution EPR measurements were performed using a quartz flat cell. A tungsten-halogen lamp and water filter were used to illuminate Cu_2O solutions. Room temperature CW X-band EPR measurements were performed

for Cu_2O nanoparticles to characterize any copper signals that may be present. The low temperature EPR spectra of the solutions of the precursor Cu(I)−TEA (100 mM) and the EPR-standard $CuSO_4$ (100 μM) were also recorded that allowed the estimation of the proportion of Cu(II) in the Cu(I)−TEA precursor sample. To estimate the proportion of Cu(II) in the Cu_2O nanoparticles, we assumed that we can quantitatively compare the powder EPR spectra recorded for the Cu_2O sample with the $CuSO_4$ standard, factoring in changes in the instrument settings and the temperature. For spin trap experiments, 20 mg of Cu_2O nanoparticles was dispersed in 2 mL of water (0.07 M). 1 mL of this solution was then mixed with 1 mL of DMPO dissolved in water (4.6 mM) in the dark. The reaction mixture was continuously stirred with a small magnetic stirrer. An aliquot of this mixture was taken prior to illumination and its EPR spectrum was recorded. The reaction vessel containing the Cu_2O/DMPO mixture was then illuminated for 15 min using cold white light and the EPR spectrum was recorded.

Photocatalytic measurement

The photocatalytic activity of the Cu_2O nanoparticles was assessed by observing their capacities to degrade MO in aqueous solutions. The photocatalytic tests were performed under cold white LED under a fixed illumination of 16 mW cm^{-2}. In each experiment, the sample (2 mg) was suspended in 20 mL of 5×10^{-5} M (C_0) MO solution. The suspension was mixed under dark conditions for 30 minutes to make sure an adsorption−desorption equilibrium was achieved before any light illumination. Afterwards, at each interval (5 minutes) of light illumination, the light-exposed solution (700 μL) was collected, followed by centrifugation at 10 000 rpm to separate the particles from the solution. The supernatant was measured using a PerkinElmer UV−Vis Lambda-365 spectrophotometer to record the MO concentration (C_0). Moreover, the stability of the photocatalyst was also evaluated by performing ten consecutive cycles of catalytic experiments. At each cycle, the used photocatalyst was collected, filtered, and dried at 60 °C followed by washing several times with ethanol for the next test.

Photoelectrochemical measurement

The Cu_2O nanoparticles were deposited on FTO coated glass substrates through an electrophoresis (EP) technique reported earlier.[53] The EP process involved transferring the Cu_2O nanoparticles (2 mg mL^{-1}) in acetone media and adding 10 mg of iodine per 5 mL of acetone. The total volume of the EP solution was 7 mL. A potential of 10 V DC was applied to the working and counter electrodes (both containing FTO coated glass substrates) for a period of 3 minutes and dried at 70 °C for 30 min. The prepared substrates were dipped in such a way as to obtain a deposition of Cu_2O nanoparticles over a 1 cm^2 surface area. PEC analysis was carried out in a quartz chamber using similar conditions reported in previous studies.[52] The PEC tests including the time-resolved photoresponse and EIS studies were carried out on an Ivium compactostat workstation using a custom-made PEC test chamber with LED light sources that isolates the device from external light. A home-

made pulse generator was employed to obtain time-resolved photoresponse signals (5 seconds on and 10 seconds off mode per cycle). The LED sources include 470 nm, 525 nm, and 663 nm, with each LED specified to an FWHM of better than 25 nm. The LEDs were used after calibrating with a PM16-140 calibrated power meter from THORLABS. An aqueous solution of 0.1 M europium(III) nitrate pentahydrate (Eu(NO$_3$)$_3$·5H$_2$O) was used as the supporting electrolyte while Ag/AgCl and Pt were used as the reference and counter electrodes, respectively. EIS was measured in an open circuit (0 V potential) with frequencies from 0.01 to 105 Hz and an amplitude of 5 mV around the tested potential.

Conflicts of interest

There are no conflicts of interest to declare.

Statement of contributions

M. S. synthesised the material and performed most of the characterisation; D. J. performed the photocatalysis studies and prepared the first draft; A. E. K., Y. M. S. and S. K. B. were involved in the PEC studies; E. D. G. and J. v. E. were involved in the optical studies; P. R. and B. C. G. were involved in the TRPL measurements; E. M. assisted with the HRTEM, EELS and EDX measurements; R. R. was involved in the XPS studies; M. J., J. L. and N. C. performed the EPR measurements and analysis; V. B. designed the study, analysed the data with other co-authors and prepared the manuscript.

Acknowledgements

References

1 Z. M. Davoudi, A. E. Kandjani, A. I. Bhatt, I. L. Kyratzis, A. P. O'Mullane and V. Bansal, *Adv. Funct. Mater.*, 2014, 24, 1047–1053.

2 A. E. Kandjani, Y. M. Sabri, M. Mohammad-Taheri, V. Bansal and S. K. Bhargava, *Environ. Sci. Technol.*, 2015, 49, 1578–1584.

3 A. Pearson, A. P. O'Mullane, V. Bansal and S. K. Bhargava, *Inorg. Chem.*, 2011, 50, 1705–1712.

4 D. D. La, R. Ramanathan, A. Rananaware, V. Bansal and S. V. Bhosale, *RSC Adv.*, 2016, 6, 33931–33936.

5 J. Schneider, M. Matsuoka, M. Takeuchi, J. Zhang, Y. Horiuchi, M. Anpo and D. W. Bahnemann, *Chem. Rev.*, 2014, 114, 9919–9986.

6 Y. Zhao, C. Tao, G. Xiao, G. Wei, L. Li, C. Liu and H. Su, *Nanoscale*, 2016, 8, 5313–5326.

7 R. Ramanathan and V. Bansal, *RSC Adv.*, 2015, 5, 1424–1429.

8 A. Pearson, H. Zheng, K. Kalantar-zadeh, S. K. Bhargava and V. Bansal, *Langmuir*, 2012, 28, 14470–14475.

9 E. Kowalska, H. Remita, C. Colbeau-Justin, J. Hupka and J. Belloni, *J. Phys. Chem. C*, 2008, 112, 1124–1131.

10 M. Mohammadtaheri, R. Ramanathan and V. Bansal, *Catal. Today*, 2016, 278, 319–329.

11 S. Sun, *Nanoscale*, 2015, 7, 10850–10882.

12 P. Basnet and Y. Zhao, *Catal. Sci. Technol.*, 2016, 6, 2228–2238.

13 H.-Y. Jing, T. Wen, C.-M. Fan, G.-Q. Gao, S.-L. Zhong and A.-W. Xu, *J. Mater. Chem. A*, 2014, 2, 14563–14570.

14 D. Jana and G. De, *RSC Adv.*, 2012, 2, 9606–9613.

15 L. Zhang and H. Wang, *ACS Nano*, 2011, 5, 3257–3267.

16 S. Ghosh, S. Saha, D. Sengupta, S. Chattopadhyay, G. De and B. Basu, *Ind. Eng. Chem. Res.*, 2017, 56, 11726–11733.

17 A. Chakravarty, K. Bhowmik, A. Mukherjee and G. De, *Langmuir*, 2015, 31, 5210–5219.

18 S. Arshadi-Rastabi, J. Moghaddam and M. Reza Eskandarian, *J. Ind. Eng. Chem.*, 2015, 22, 34–40.

19 Z. Zheng, B. Huang, Z. Wang, M. Guo, X. Qin, X. Zhang, P. Wang and Y. Dai, *J. Phys. Chem. C*, 2009, 113, 14448–14453.

20 W. Wang, D. Wu, Q. Zhang, L. Wang and M. Tao, *J. Appl. Phys.*, 2010, 107, 123717.

21 H. N. Ahmadabadi, T. Ahmed, S. Walia, R. Ramanathan, A. Kandjani, S. Rubanov, J. Kim, O. Kavehei, V. Bansal, M. Bhaskaran and S. Sriram, *Nanotechnol.*, 2016, 27, 505210.

22 T. Ahmed, S. Walia, J. Kim, H. Nili, R. Ramanathan, E. L. H. Mayes, D. W. M. Lau, O. Kavehei, V. Bansal, M. Bhaskaran and S. Sriram, *Nanoscale*, 2017, 9, 14690–14702.

23 J. Liu, J. Ke, D. Li, H. Sun, P. Liang, X. Duan, W. Tian, M. O. Tadé, S. Liu and S. Wang, *ACS Appl. Mater. Interfaces*, 2017, 9, 11678–11688.

24 S. E. Repper, A. Haynes, E. J. Ditzel and G. J. Sunley, *Dalton Trans.*, 2017, 46, 2821–2828.

25 Y. Kwon, A. Soon, H. Han and H. Lee, *J. Mater. Chem. A*, 2015, 3, 156–162.

26 D. M. Antonelli and J. Y. Ying, *Angew. Chem., Int. Ed. Engl.*, 1996, 35, 426–430.

27 J. T. Yoke, J. F. Weiss and G. Tollin, *Inorg. Chem.*, 1963, 2, 1210–1216.

28 J. F. Weiss, G. Tollin and J. T. Yoke, *Inorg. Chem.*, 1964, 3, 1344–1348.

29 W. E. Hatfield and J. T. Yoke, *Inorg. Chem.*, 1962, 1, 463–470.

30 R. Ji, W. Sun and Y. Chu, *RSC Adv.*, 2014, 4, 6055–6059.

31 Y. Wang, S. Lany, J. Ghanbaja, Y. Fagot-Revurat, Y. P. Chen, F. Soldera, D. Horwat, F. Mücklich and J. F. Pierson, *Phys. Rev. B*, 2016, 94, 245418.

32 L. Wu, J. Yang, M. Chi, S. Wang, P. Wei, W. Zhang, L. Chen and J. Yang, *Sci. Rep.*, 2015, 5, 14319.

33 A. Paolella, R. Brescia, M. Prato, M. Povia, S. Marras, L. De Trizio, A. Falqui, L. Manna and C. George, *ACS Appl. Mater. Interfaces*, 2013, 5, 2745–2751.

34 L. Yang, J. Lv, Y. Sui, W. Fu, X. Zhou, J. Ma, S. Su, W. Zhang, P. Lv, D. Wu, Y. Mu and H. Yang, *CrystEngComm*, 2014, 16, 2298–2304.

35 C. Garlisi, G. Scandura, J. Szlachetko, S. Ahmadi, J. Sa and G. Palmisano, *Appl. Catal., A*, 2016, 526, 191–199.

36 L. Debbichi, M. C. Marco de Lucas, J. F. Pierson and P. Krüger, *J. Phys. Chem. C*, 2012, 116, 10232–10237.

37 Y. Mao, J. He, X. Sun, W. Li, X. Lu, J. Gan, Z. Liu, L. Gong, J. Chen, P. Liu and Y. Tong, *Electrochim. Acta*, 2012, 62, 1–7.

38 S. Wu, Z. Yin, Q. He, G. Lu, X. Zhou and H. Zhang, *J. Mater. Chem.*, 2011, 21, 3467–3470.

39 A. Chowdhury, P. K. Bijalwan and R. K. Sahu, *Appl. Surf. Sci.*, 2014, 289, 430–436.

40 H. Shi, K. Yu, Y. Wang, Q. Wang and Z. Zhu, *Appl. Phys. A*, 2012, 108, 709–717.

41 H. Shi, K. Yu, F. Sun and Z. Zhu, *CrystEngComm*, 2012, 14, 278–285.

42 S. Mandeep, G. Enrico Della, A. Taimur, W. Sumeet, R. Rajesh, E. Joel van, M. Edwin and B. Vipul, *2D Mater.*, 2017, 4, 025110.

43 A. Pearson, S. K. Bhargava and V. Bansal, *Langmuir*, 2011, 27, 9245–9252.

44 A. Pearson, H. Jani, K. Kalantar-zadeh, S. K. Bhargava and V. Bansal, *Langmuir*, 2011, 27, 6661–6667.

45 A. Pearson, S. Bhosale, S. K. Bhargava and V. Bansal, *ACS Appl. Mater. Interfaces*, 2013, 5, 7007–7013.

46 S. R. Anderson, M. Mohammadtaheri, D. Kumar, A. P. O'Mullane, M. R. Field, R. Ramanathan and V. Bansal, *Adv. Mater. Interfaces*, 2016, 3, 1500632–n/a.

47 M. Jahurul Islam, D. Amaranatha Reddy, N. S. Han, J. Choi, J. K. Song and T. K. Kim, *Phys. Chem. Chem. Phys.*, 2016, 18, 24984–24993.

48 Y. Su, A. Nathan, H. Ma and H. Wang, *RSC Adv.*, 2016, 6, 78181–78186.

49 S. Kumar, C. M. A. Parlett, M. A. Isaacs, D. V. Jowett, R. E. Douthwaite, M. C. R. Cockett and A. F. Lee, *Appl. Catal., B*, 2016, 189, 226–232.

50 Y.-C. Pu, H.-Y. Chou, W.-S. Kuo, K.-H. Wei and Y.-J. Hsu, *Appl. Catal., B*, 2017, 204, 21–32.

51 L. Xu, F. Zhang, X. Song, Z. Yin and Y. Bu, *J. Mater. Chem. A*, 2015, 3, 5923–5933.

52 A. E. Kandjani, Y. M. Sabri, M. R. Field, V. E. Coyle, R. Smith and S. K. Bhargava, *Chem. Mater.*, 2016, 28, 7919–7927.

53 R. Abe, M. Higashi and K. Domen, *J. Am. Chem. Soc.*, 2010, 132, 11828–11829.